

pubs.acs.org/JACS Article

Substituent Impact on Quinoxaline Performance and Degradation in **Redox Flow Batteries**

Sanat Vibhas Modak, Daniel Pert, Jessica L. Tami, Wanggang Shen, Ibrahim Abdullahi, Xun Huan, Anne J. McNeil, Bryan R. Goldsmith, and David G. Kwabi*



Cite This: J. Am. Chem. Soc. 2024, 146, 5173-5185



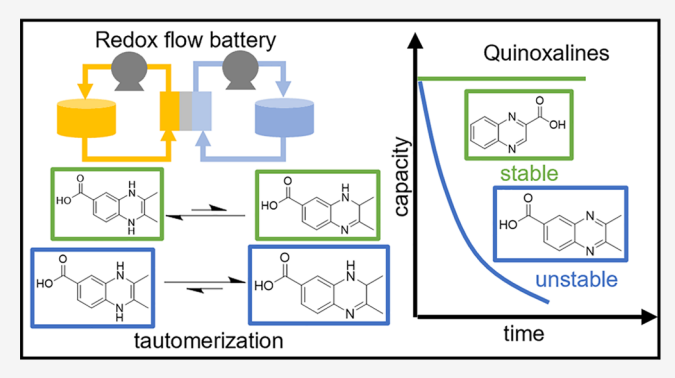
ACCESS I

Metrics & More

Article Recommendations

Supporting Information

ABSTRACT: Aqueous redox flow batteries (RFBs) are attractive candidates for low-cost, grid-scale storage of energy from renewable sources. Quinoxaline derivatives represent a promising but underexplored class of charge-storing materials on account of poor chemical stability in prior studies (with capacity fade rates >20%/day). Here, we establish that 2,3-dimethylquinoxaline-6carboxylic acid (DMeQUIC) is vulnerable to tautomerization in its reduced form under alkaline conditions. We obtain kinetic rate constants for tautomerization by applying Bayesian inference to ultraviolet-visible spectroscopic data from operating flow cells and show that these rate constants quantitatively account for capacity fade measured in cycled cells. We use density functional theory (DFT) modeling to identify structural and chemical predictors of



tautomerization resistance and demonstrate that they qualitatively explain stability trends for several commercially available and synthesized derivatives. Among these, quinoxaline-2-carboxylic acid shows a dramatic increase in stability over DMeQUIC and does not exhibit capacity fade in mixed symmetric cell cycling. The molecular design principles identified in this work set the stage for further development of quinoxalines in practical, aqueous organic RFBs.

1. INTRODUCTION

There has been widespread proliferation of renewable energy conversion systems over the past decade, especially solar and wind power installations. However, given the intermittent availability of solar and wind power, low-cost energy storage technology is required to meet mismatches in energy supply versus demand and encourage more widespread grid-scale penetration of these resources. Redox flow batteries (RFBs) are promising technologies for low-cost energy storage. RFBs store energy in redox-active charge carriers dissolved in a pair of electrolytes, termed the negative and positive electrolytes, separated by a membrane. These electrolytes are stored in separate reservoirs and pumped through an electrochemical reactor, where redox reactions store or release electrical energy. This architecture decouples the energy storage and power capacities of the RFB, with the former scaling with the volume and concentration of the charge carriers in their respective electrolytes, and the latter scaling with the reactor's conductance and electrode area. An RFB's cost (\$/kW·h) approaches the cost of its electrolytes as its discharge duration (ratio of energy to power) increases, i.e., as electrolyte's energy storage capacity increases for a fixed power capacity.^{2,3} RFBs therefore may provide cheaper energy storage compared to solid-state batteries if sufficiently inexpensive charge carriers are developed.4

Several classes of aqueous-soluble organic molecules have been investigated as potential low-cost charge carriers in RFBs.^{3,5} Unfortunately, most of these molecules undergo rapid decomposition (resulting in a capacity loss rate during flow cell cycling of 0.1%/day or higher) through various pathways. In recent years, considerable progress has been made with certain substituted anthraquinones^{7–10} and phenazines^{11–13} as negative electrolyte molecules, where low (ca. ≤ 0.01%/day) capacity fade rates have been measured against ferrocyanide (Fe(CN)₆)-based positive electrolytes under alkaline conditions. Drawbacks to many of these molecular pairings include low open-circuit voltages (around 1.0 V) and high anticipated raw material and synthetic costs. Techno-economic analyses 14,15 project that the costs of energy storage systems that contain these molecules will exceed the \$150/kW·h target set by the U.S. Department of Energy, 16 and it is worth noting that this target has been deemed by some to be too high for successful commercialization. There is clearly a need for

Received: September 28, 2023 Revised: January 18, 2024 Accepted: January 19, 2024 Published: February 15, 2024





further exploration of the organic chemistry design space for more suitable redox-active molecules. Gregory et al. 15 proposed developing redox-active molecules with extreme redox potentials (leading to open-circuit voltages $\geq 1.5~\rm V$), low equivalent weights (<100 g per mole e $^-$ stored), and abundant precursors to meet the RFB design needs.

Quinoxalines are an underexplored but promising class of negative electrolyte molecules in this respect because many derivatives have lower redox potentials 19-22 and higher solubilities 19,23,24 than typical anthraquinones and phenazines. The equivalent weight of quinoxaline (65 g/mol) is also lower than that of anthraquinone (104 g/mol) and phenazine (90 g/ mol), and many substituted quinoxalines are straightforward to synthesize in one-step reactions using widely available precursors. ^{25–27} Like anthraquinones and phenazines, quinoxalines undergo a two-electron redox reaction. 11,28 Although they are known to be viable charge carriers in nonaqueous flow batteries, 29-32 studies which have explored the cycling behavior of aqueous flow cells containing quinoxalines 20,33,32 reported rapid capacity fade, equivalent to >20%/day. Progress in developing more stable aqueous-soluble quinoxalines is hindered because the connection between capacity fade and molecular decomposition mechanisms and rates is not well understood. For example, although reduced quinoxalines are known to undergo tautomerization, 35-37 their impact on capacity retention in flow cells is unclear. A recent study suggested quinoxaline dimerization as the primary degradation mechanism driving capacity fade in alkaline electrolytes.²⁰ Other reports have proposed Michael attack or irreversible hydrogenation as possible decomposition mechanisms.^{38,39}

In this study, we investigate the relationship between capacity fade in aqueous quinoxaline-based RFBs and molecular decay by combining flow cell cycling with a suite of chemical analysis techniques, including ultraviolet-visible (UV-vis) spectroscopy, nuclear magnetic resonance (NMR) spectroscopy, and mass spectrometry. Using 2,3-dimethylquinoxaline-6-carboxylic acid (DMeQUIC) as a model quinoxaline, our analysis reveals that tautomerization of the reduced form of quinoxalines is primarily responsible for capacity fade rather than Michael addition, dimerization, or hydrogenation. By subjecting spectroscopic data obtained from operating flow cells to a Bayesian statistical inference protocol, we calculate the rate constant of tautomerization and show that it quantitatively explains fade rates observed in cycled cells. Using DFT calculations, we rationalize trends in the tautomerization energetics of quinoxaline derivatives and suggest molecular design rules. We identify a more tautomerization-resistant quinoxaline-2-carboxylic acid (2QUIC) that did not exhibit capacity fade for 220 h of flow cell cycling in a mixed symmetric configuration.

2. MATERIALS AND METHODS

2.1. Chemicals. Sodium ferrocyanide (>98%), sodium hydroxide (>99%), and sodium chloride (>99%) were purchased from Sigma-Aldrich. 2,3-Dimethyl-quinoxaline-6-carboxylic acid (>97%), quinoxaline-6-carboxylic acid (>95%), 2,3-dimethylquinoxaline (>97%), quinoxaline-2-carboxylic acid (>97%), 2,3-bis(bromomethyl)-quinoxaline (>97%), 3-amino-quinoxaline-2-carboxylic acid (QUI2C3A), sodium sulfite (98%), 3,4-diaminobenzoic acid (>97%), glyoxal sodium bisulfite (98%), dimethyl sulfoxide, and ethanol (absolute) were purchased from Fisher Scientific and used as received. Methanesulfonic acid-deuterium and methanesulfonic acid-sodium salt were purchased from Sigma-Aldrich and used as received. 2,3-Dimethyl-1,2,3,4-tetrahydro-quinoxaline-6-carboxylic acid was

used as received from 1 ClickChemistry. All electrolyte solutions were made with deionized water (18 $M\Omega\text{-cm}).$

- **2.2. Ultraviolet–Visible Spectroscopy.** UV–vis spectroscopy was conducted on an Ocean-HDX-UV–VIS spectrometer HDX00518 (Ocean Insight). Spectroscopic measurements were taken using 50 and 25 ms integration times for the ex situ and operando experiments, respectively, and averaged over 50 scans in both cases. The operando UV–vis cross-flow cell was purchased from Firebird Optics and had a path length of 60 μ m. Unless otherwise noted, all ex situ measurements were conducted at a nominal 0.1 mM concentration of the active material in a supporting electrolyte of 3 M NaOH.
- **2.3. Cyclic Voltammetry.** Three-electrode cyclic voltammetry (CV) of all charge carriers studied in this work was conducted in 3 M NaOH, unless specified otherwise, using a 5 mm diameter glassy carbon disk electrode (Basi Inc.) along with a Ag/AgCl reference electrode (BaSI Inc.) and Pt wire (Basi Inc.) as the counter electrode at a scan rate of 50 mV/s. All CVs were conducted at a nominal active material concentration of 1 mM using a CH Instruments CHI7013E potentiostat. The CVs were performed with an 85% resistance compensation.
- 2.4. Flow Cell Preparation and Cycling. Flow cells were constructed with hardware from Fuel Cell Technologies (Albuquerque, New Mexico) and assembled in a zero-gap configuration, similar to previous reports. 40,41 Pyrosealed POCO graphite flow plates with serpentine flow patterns were used for both electrodes, and 50 μ m-thick Nafion 212 (Fuel Cell Store) was used as the membrane. Each electrode comprised a 5 cm² sheet of CE Tech GF020 graphite felt (Fuel Cell Store, 2.1 mm thick). The electrodes were oven-dried in air for 12 h at 400 °C prior to use, whereas membranes were pretreated by being soaked in the supporting electrolyte for 24 h before use in the cell. The electrodes and membrane were held in place using Viton sheets with the 5 cm² electrode area cut out. The torque applied during cell assembly was 13 Nm on each of the eight bolts. A Longer DG-15 peristaltic pump, Cole Parmer SK-77202-60 peristaltic pump or KNF NFB30 diaphragm pump circulated the electrolytes through the flow cell through fluorinated ethylene propylene tubing (inner diameter = 1/16 in.) sourced from McMaster Carr. Calibration curves were obtained for each pump that permitted translation from the control voltage to a volumetric flow rate in mL/ min. A flow rate of 50 mL/min was used in the cell cycling and operando flow cell experiments. All flow cells for which operando UV-vis measurements were not performed were cycled in a nitrogen glovebox with ≤ 2 ppm of O_2 . We degassed the electrolytes prior to cycling by exposing them to the glovebox's nitrogen atmosphere for 1 h. The operando flow cell experiments were conducted outside the glovebox, but the negative electrolyte was protected from atmospheric oxygen by maintaining a blanket of nitrogen gas in the headspace.

Sodium ferrocyanide $(Na_4Fe(CN)_6)$ was used in the non-capacity-limiting electrolyte in all of our compositionally asymmetric cells. Unless otherwise noted, cycling experiments were performed using a constant-current, constant-voltage cycling protocol to access the entire capacity of the capacity-limiting electrolyte. ⁴² In this protocol, a constant current is applied to the cell until a specified potential limit is reached; the cell is then held at that potential until the current density reaches an absolute value of 1 mA/cm². A Biologic VSP potentiostat was used for cell cycling measurements.

- **2.5. Permeability Measurements.** Membrane permeability was measured using a homemade glass H-cell with a liquid volume of 6 mL on each side arm along with Viton gaskets to hold the membrane with an opening of 0.9 cm². The donating side was filled with the charge carrier and supporting electrolyte, whereas the receiving side contained the supporting electrolyte only. The concentration of crossed-over material in the receiving side was characterized using UV—vis spectrophotometry, and the permeability was calculated from the slope of crossed over concentration versus time based on Fick's law.
- **2.6.** Synthesis of Sodium 2,3-Bismethylsulfonate (DMeSQUI). DMeSQUI was synthesized following a previously reported procedure (Figure S1).²⁰ We stirred 2,3-bis(bromomethyl)-

quinoxaline (0.632 g, 2 mmol) in dimethyl sulfoxide (DMSO, 6 mL) and aqueous 1.1 M $\rm Na_2SO_3$ (4 mL) at 100 °C for 16 h in a sealed vial. The resulting solution was then cooled to room temperature and filtered through filter paper. The filtrate volume was reduced to 5 mL by evaporation by heating the solution, and then ethanol (50 mL) was added. The resulting suspension was filtered using filter paper, and the white precipitate was collected and dried. The $^1 H$ NMR spectrum of DMeSQUI is shown in Figure S2 and its CV in Figure S3.

2.7. Mass Spectrometry and NMR Spectroscopy. Mass spectrometry was performed using an Agilent 6230 TOF Mass spectrometer with a C18 column on samples diluted to 100 μ M in water with an injection volume of 20 μ L. All measurements were carried out in negative ion mode.

All ^1H and ^{13}C NMR spectra were acquired at room temperature in deuterated solvents using a Bruker Avance Neo 500. ^1H NMR spectra were taken using a 2 s relaxation delay, and ^{13}C NMR spectra had a 1 s relaxation delay. All chemical shifts are reported in units of $\delta(\text{ppm})$ relative to tetramethylsilane (TMS) and referenced to residual solvent. Peak multiplicities were reported in the following manner: singlet (s), doublet (d), doublet of doublets (dd), triplet (t), quartet (q), multiplet (m), and broad signal (br). We used a solution of 0.1 M NaOD and 0.05 M CH₃SO₃Na or CH₃SO₃D (as specified for each experiment) in D₂O as the internal standard. For all our NMR measurements, we mixed 150 μL of the sample solution with 600 μL of the internal standard by volume, and 600 μL of the resulting solution was put into the NMR tube.

2.8. Bayesian Inference. Upon reduction, DMeQUIC converts to rDMQ, which is understood to decompose into a transient, redoxactive intermediate, tDMQ, and a final, redox-inactive form, fDMQ

$$DMeQUIC \xrightarrow{k_0} rDMQ \xrightarrow{k_1} tDMQ \xrightarrow{k_2} fDMQ$$
 (1

Assuming first-order kinetics, the reactions can be described by the following equations

$$\frac{\text{d[DMeQUIC]}}{\text{d}t} = -k_0[\text{DMeQUIC}] \tag{2}$$

$$\frac{\mathrm{d[rDMQ]}}{\mathrm{d}t} = k_0[\mathrm{DMeQUIC}] - k_1[\mathrm{rDMQ}] \tag{3}$$

$$\frac{\text{d[tDMQ]}}{\text{d}t} = k_1[\text{rDMQ}] - k_2[\text{tDMQ}]$$
(4)

$$\frac{\mathrm{d[fDMQ]}}{\mathrm{d}t} = k_2[\mathrm{tDMQ}] \tag{5}$$

where k_0 , k_1 , and k_2 are rate constants that are unknown and of interest. The pure spectra (i.e., molar absorption coefficient at each wavelength) of rDMQ, tDMQ, and fDMQ (denoted hereafter as $S_{\rm rDMQ}$, $S_{\rm tDMQ}$, and $S_{\rm fDMQ}$, respectively) are also unknown. Note that the pure spectrum of DMeQUIC (i.e., $S_{\rm DMeQUIC}$) is known because the initial concentrations of all of the other species (i.e., prior to DMeQUIC reduction) are equal to zero.

We use θ to denote the collection of unknown parameters (rate constants and pure spectra) and y_t to denote the observations (absorbance at time t). Following the Beer–Lambert law, the observation model is

$$\begin{aligned} y_t &= G(\theta; S_{\text{DMeQUIC}}, t) + \epsilon \\ &= [\text{DMeQUIC}]_t S_{\text{DMeQUIC}} + [\text{rDMQ}]_t S_{\text{rDMQ}} \\ &+ [\text{tDMQ}]_t S_{\text{tDMQ}} + [\text{fDMQ}]_t S_{\text{fDMQ}} + \epsilon \end{aligned}$$

where the path length term is factored out. Here, $[DMeQUIC]_p$ $[rDMQ]_p$ $[tDMQ]_p$ and $[fDMQ]_t$ are the concentrations solved by the reaction kinetics at time t, and ϵ is a noise term that follows a zero-mean Gaussian distribution $\mathcal{N}(0, \Sigma_\epsilon)$, where Σ_ϵ is a diagonal matrix with the identical entry 0.01^2 on the diagonal. The noise term represents the discrepancy between model prediction and experimental observation that may arise due to, for example, measurement

variability and other factors not represented by the model. The probability density function (PDF) of likelihood for observing y_t given underlying parameters being θ can be evaluated as $p(y_t|\theta) = p_e(y_t - G(\theta; S_{\text{DMeQUIC}}, t))$

$$= \mathcal{N}(y_t - G(\theta; S_{\text{DMeQUIC}}, t); 0, \Sigma_{\epsilon})$$

After the spectroscopic data is obtained, the uncertainty on unknown parameters θ can be updated via Bayes' rule

$$p(\theta|y) = \frac{p(y|\theta)p(\theta)}{p(y)} \propto p(y|\theta)p(\theta)$$
(7)

where $p(\theta)$ is the prior PDF (i.e., the uncertainty before incorporating the observed data), $p(\theta|y)$ is the posterior PDF (i.e., the updated uncertainty after incorporating the observed data), p(y) is the model evidence (also known as the marginal likelihood) which is a constant with respect to parameters θ , and $p(y|\theta)$ is the likelihood PDF described earlier. Assuming the independence of noise terms, the overall likelihood PDF can be factored to be the product of each data point's individual likelihood

$$p(y|\theta) = \prod_{t} p(y_t|\theta)$$
(8)

We also adopt a Bayesian prior PDF that starts with all unknown parameters being independent

$$p(\theta) = p(k_0)p(k_1)p(k_2)p(S_{\text{rDMQ}})p(S_{\text{tDMQ}})p(S_{\text{fDMQ}})$$
(9)

where the prior of the logarithmic reaction rates follows a non-informative uniform distribution, i.e., $\log_{10}k \sim \mathcal{U}[-6,0]$ for all k terms. We note that the independence assumption is only in the prior, and any dependence structure emerges in the posterior once data is incorporated. The prior distribution for the unknown pure spectra is chosen to incorporate three essential characteristics: (1) nonnegativity of absorbance values, (2) a decreasing overall trend of absorbance values from low to high wavelengths, and (3) the smoothness of the spectrum. Therefore, the prior of the unknown pure spectra is selected as a half-normal distribution (or equivalently, a zero-mean-normal distribution truncated below zero) with a decreasing standard deviation. Moreover, additional penalties on the first-order and second-order derivatives of the spectrum are incorporated into the prior to ensure smoothness. The prior PDF of spectrum S for $S \in \{S_{\text{FDMQ}}, S_{\text{FDMQ}}, S_{\text{FDMQ}}\}$ can be represented as

$$p(S) = \prod_{i} \mathcal{HN}(S_{i}; \sigma_{i}) \times \underbrace{\mathcal{N}(\delta S_{i}; 0, 0. 002^{2})}_{\text{penalty on first-order derivative}} \times \underbrace{\mathcal{N}(\delta^{2} S_{i}; 0, 0. 002^{2})}_{\text{penalty on second-order derivative}}$$
(10)

where i is the index of spectrum grid, \mathcal{HN} represents the half-normal distribution, and σ_i linearly decreases from 0.2 at the lowest wavelength to 0.001 at the highest wavelength (i.e., decreases from 0.2 at minimal i to 0.001 at maximal i). The first-order difference δS_i and the second-order difference $\delta^2 S_i$ are calculated using the finite difference method.

Because θ (capturing all unknown model parameters) is high dimensional due to the inclusion of unknown spectra (i.e., absorbance values recorded at each wavelength), estimating posteriors with grid discretization is impractical. We use Markov chain Monte Carlo (MCMC)^{43,44} to sample from the posterior instead. In particular, we utilize the Metropolis–Hastings algorithm^{45,46} implemented in PyMC3⁴⁷ for this purpose. It is important to highlight that the inclusion of penalty terms in eq 10 significantly enhances the smoothness of the sampled spectra. Without these penalty terms, the sampled spectra would exhibit a highly oscillatory pattern. These penalty terms, however, are solely included for the purpose of regularizing posterior sampling. Once the samples are obtained, their posterior probabilities are re-evaluated without the penalty terms.

Unlike our previous work, 48 this work does not involve Bayesian model selection because of the much higher dimensionality of

unknown parameters caused by the involvement of unknown spectra (i.e., UV—vis absorbance at each wavelength recorded, amounting to 2068 unknown absorbance values at each time step). Therefore, a vast number of samples would be required to accurately estimate the evidence term, where most would contribute near-zero likelihood values.

2.9. Density Functional Theory Modeling. Density functional theory (DFT) calculations were used to predict energies for tautomerization, Michael attack, and dimerization, as well as redox potentials and p K_a values of various quinoxaline derivatives. All DFT calculations were performed using the NWChem software with the B3LYP exchange—correlation functional 50,51 and the Def2-TZVPPD basis set. The COSMO implicit solvation model with default parameters was used during geometry optimization to implicitly treat molecule solvation by water. 53,54 A self-consistent field convergence energy of 1×10^{-6} au was used. To maintain charge neutrality, we model carboxylic and sulfonic acid functional groups without deprotonation.

The following equations were used to calculate the Gibbs free energies of reduction (ΔG_{red}) and tautomerization (ΔG_{taut})

$$\Delta G_{\text{red}} = G_{\text{enamine}} - G_{\text{H}_2} - G_{\text{oxidized}} \tag{11}$$

$$\Delta G_{\text{taut}} = G_{\text{imine}} - G_{\text{enamine}} \tag{12}$$

where $G_{\rm enamine}$, $G_{\rm imine}$, and $G_{\rm oxidized}$ are the DFT-calculated Gibbs free energies of the enamine form ${\bf i}$, imine form ${\bf iv}$ (see Figure S4), and oxidized form of the given quinoxaline. The p $K_{\rm a}$ values of the imine and enamine forms of quinoxaline derivatives were calculated as follows

$$pK_{\rm a} = \frac{1}{RT \ln(10)} (G_{\rm X} + G_{\rm H} + G_{\rm HX})$$
(13)

where $G_{\rm X}^-$, $G_{\rm HX}$, and $G_{\rm H}^+$ are the Gibbs free energies of the deprotonated species, protonated species, and solvated proton, respectively. R is the ideal gas constant, and T is the temperature (298.15 K). The Gibbs free energy of the solvated proton ($G_{\rm H}^+$) was estimated as -270.0 kcal/mol using the average value obtained via the direct method based on the experimental p $K_{\rm a}$ values of ammonium, acetic acid, chloroacetic acid, and trichloroacetic acid (9.25, 4.76, 2.86, and 0.70, respectively) and the DFT-calculated free energies of the conjugate acid and base ($G_{\rm H}^+ = -267.4$, -275.2, -271.7, and -265.8 kcal/mol, respectively).

Gibbs free energies were estimated at 298.15 K and 1 M species by correcting the DFT-calculated electronic energies for enthalpic and entropic effects

$$G = E_{\text{elec}} + H_{\text{thermal}} - TS_{\text{aq}} \tag{14}$$

where $E_{\rm elec}$ and $H_{\rm thermal}$ are the DFT-calculated electronic energy and the thermal correction to enthalpy, which includes contributions from the zero-point energy and heat capacity. The aqueous-phase entropy $S_{\rm aq}$ was estimated from the gas-phase entropy $S_{\rm gas}$ using the following equation, which accounts for solvent-induced structural order that changes the translational entropy of species in solution 56

$$S_{\rm aq} = S_{\rm gas} - 0.46 \left(S_{\rm gas} - 14.3 \frac{\text{cal}}{\text{mol} \cdot \text{K}} \right)$$
 (15)

Vibrational frequencies within the harmonic approximation were calculated using finite differences and used to determine H_{thermal} and S_{gas} .

 $S_{\rm gas}$. The standard redox potential (E^0) at pH 13 was calculated using the Nernst equation

$$E^{0} = -\frac{\Delta G_{\text{red}}}{nF} - \frac{2RT}{nF \log_{10}(e)} \cdot \text{pH}$$
(16)

where n is the number of electrons transferred (n = 2 for our study), F is Faraday's constant, and e is Euler's number. Additional details on computing Michael attack and dimerization energetics are given in the Supporting Information.

3. RESULTS AND DISCUSSION

3.1. Flow Cell Cycling of DMeQUIC. DMeQUIC was chosen as a model quinoxaline for several reasons. First, it has a low reduction potential (-1.09 vs Ag/AgCl at pH 13), leading to high open-circuit potentials against certain common positive electrolyte charge carriers: 1.37 V against ferrocyanide (Figure 1) and 1.55 V against permanganate. ^{57–61} Second, from cyclic

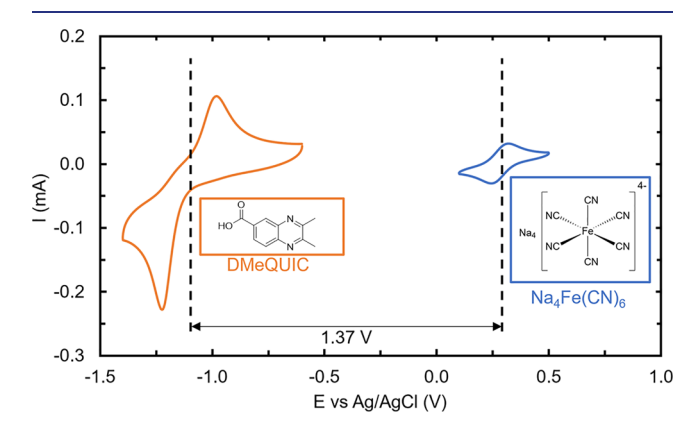


Figure 1. Cyclic voltammograms of 1 mM DMeQUIC and sodium ferrocyanide performed at a scan rate of 50 mV/s in an aqueous supporting electrolyte of 0.1 M NaOH and 1 M NaCl (pH 13).

voltammogram (CV) measurements, it has moderately fast redox kinetics, with a 260 mV separation between cathodic and two anodic redox peaks at a scan rate of 50 mV/s. Third, it is commercially available.

We cycled 0.4 M DMeQUIC against excess sodium ferrocyanide in an alkaline (pH 13) flow cell at 20 mA cm⁻² using a constant current-constant voltage (CCCV) protocol and found that the current efficiency and rate of capacity fade were strongly dependent on the potential limit applied on discharge (Figure 2). During the first cycle (Figure 2a), two voltage plateaus were present upon discharge, centered at ca. 1.1 and 0.0 V. About 40% of the charging (DMeQUIC reduction) capacity was recovered at the higher plateau, and the remaining capacity was recovered at or below the lower plateau. These data suggest that the reduced form of DMeQUIC decomposed into at least one product that can be converted back to DMeQUIC at a high oxidative overpotential. These potential-dependent variations in current efficiency manifested as differences in capacity retention during long-term CCCV cycling (Figure 2b)—cycling at a discharge potential limit of 1.0 V (shallow discharge) yielded a 90% loss of capacity within 5 h, whereas a similar capacity loss took about 60 h for cycling at a limit of -0.1 V (deep discharge). UV-vis (Figure S5a,b) and voltammetric (Figure S5c,d) analysis of the cycled DMeQUIC electrolytes revealed a clear change in chemical composition and diminution in the redox activity, respectively, indicating that the capacity fade observed in Figure 2b originated from the decomposition of and loss of redox activity in the DMeQUIC electrolyte.

The decomposition of the reduced form of DMeQUIC and its recovery upon deep discharge were supported by operando UV-vis (Figure 3a-c) and ex situ ¹H NMR (Figure 3d-f) spectroscopic data. Reduction (charging) of DMeQUIC resulted in distinct shifts in its UV-vis absorbance (Figure 3b) and ¹H NMR (Figure 3e) spectra. The NMR spectrum of the charged electrolyte suggests at least two components, consistent with reduced DMeQUIC and at least one

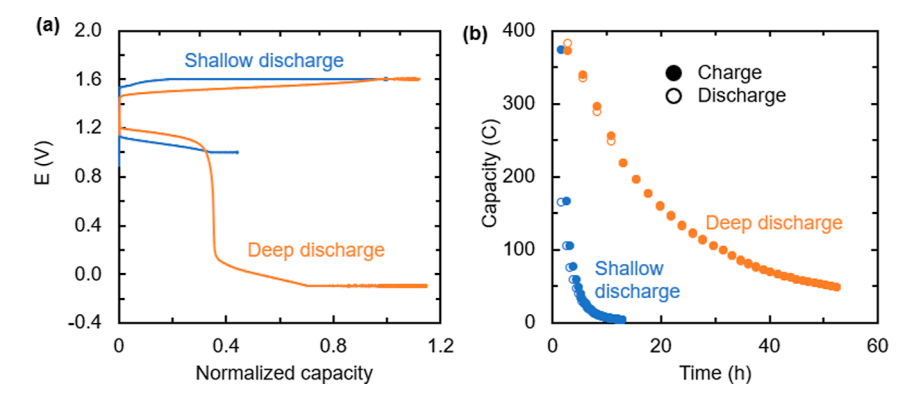


Figure 2. Flow cell cycling of DMeQUIC. (a) Potential vs capacity for shallow discharge (1.0 V discharge limit) and deep discharge (-0.1 V discharge limit) cycling. (b) Charge and discharge capacities vs time during shallow- and deep-discharge CCCV cycling at 20 mA/cm². The cells were charged to 1.6 V, and potential holds were applied until the current density fell to an absolute value of 1 mA/cm². The capacity-limiting side comprised 5 mL of 0.4 M DMeQUIC and 0.5 M NaOH, whereas the non-capacity-limiting side comprised 20 mL of 0.4 M Na₄Fe(CN)₆ and 0.1 M NaOH.

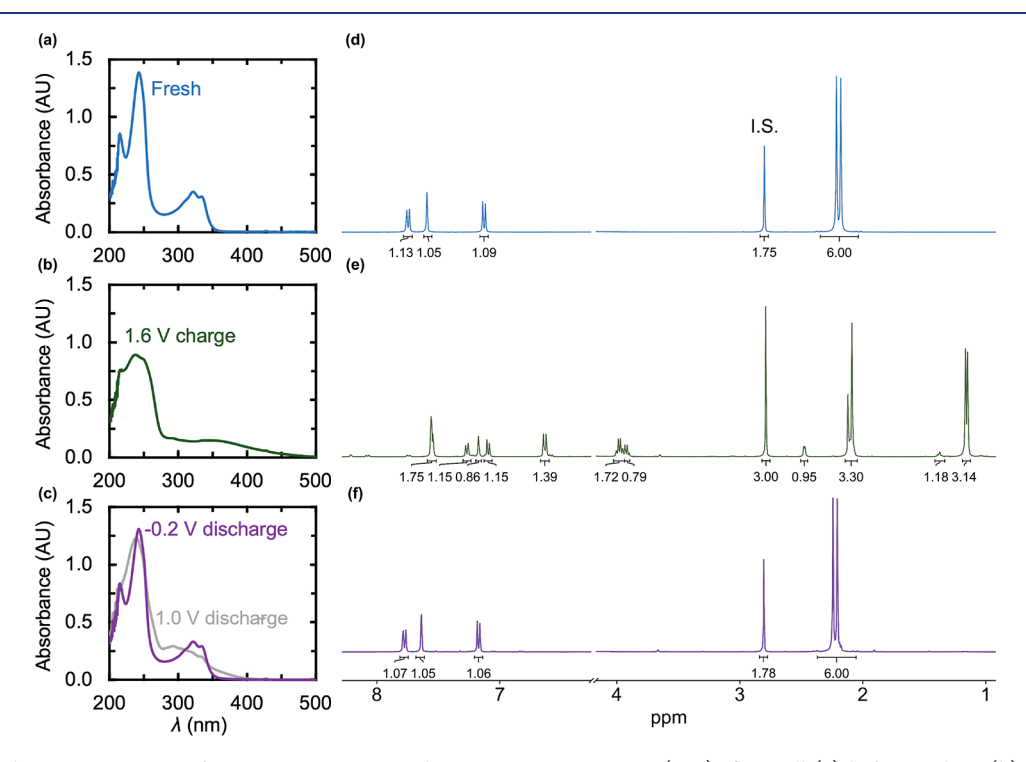


Figure 3. Operando UV—vis spectra of a 5 mM DMeQUIC solution in a DMeQUIC-Fe(CN) $_6$ flow cell (a) before cycling, (b) after charging the cell (reducing DMeQUIC) at 1.6 V and subsequently (c) discharging the cell at -0.2 or 1.0 V. Ex situ 1H NMR spectra of (d) uncycled DMeQUIC solution, (e) DMeQUIC solution after reduction at 1.6 V, and (f) DMeQUIC solution after reduction followed by oxidation at a cell potential of -0.2 V. For each NMR measurement, 0.15 mL aliquots from the 400 mM DMeQUIC electrolyte were diluted by a factor of 5 with D_2O , and CH_3SO_3Na was added as a calibration standard.

decomposition product. DMeQUIC displays two singlet peaks at ca. 2.1 ppm, originating from the pair of methyl groups at the 2 and 3 positions of the pyrazine core, which each integrate to 3H. In the aromatic region of the spectrum, there are three peaks at 7.4 ppm (doublet), 7.0 ppm (singlet), and 7.6 ppm (doublet), together integrating to three protons, as expected for this substitution pattern. These peaks should be retained, but shifted, in the reduced (charged) form, with the addition of two N–H protons, which may not show due to exchange with the deuterated NMR solvent. Instead, the methyl groups become more differentiated, with one appearing at 2.0 ppm (similar to DMeQUIC) and another more upfield at 1.0 ppm, indicating that the latter is in a new chemical environment. In

addition, there are new peaks at 3.8 ppm, which we believe correspond to new protons at the 2 and 3 positions on the pyrazine core (which are not present in reduced DMeQUIC). The aromatic region shows five peaks, providing further evidence for two or more degradation products. The original UV—vis and NMR spectra for DMeQUIC are recovered after discharge at -0.2 V (Figure 3c,f) but not at 1.0 V (Figure 3c).

3.2. Mechanistic Analysis of DMeQUIC Decomposition. We sought to understand the kinetics of DMeQUIC decomposition by combining operando UV—vis spectroscopy with Bayesian inference. Our previous work demonstrated that Bayesian statistical analysis of UV—vis data from operating organic flow cells can identify the individual spectra of

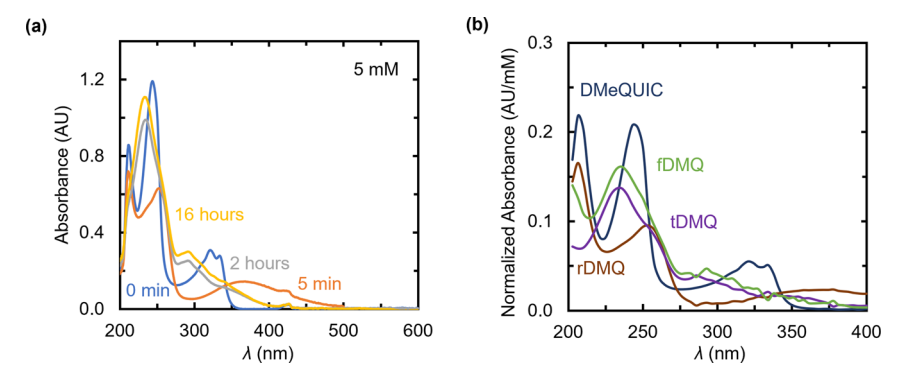


Figure 4. (a) UV-vis spectra of 5 mM DMeQUIC after 0 min, 5 min, 2 h, and 16 h of potentiostatic reduction in a DMeQUIC-Fe(CN)₆ flow cell at 1.6 V. (b) Spectra of rDMQ, tDMQ, and fDMQ estimated using Bayesian inference, displayed alongside the authentic spectrum of DMeQUIC. The lines depict the Bayesian posterior mode, whereas the posterior uncertainty (standard deviation) has been substantially reduced and is not visible in the plot.

decomposition products and their respective rate(s) of evolution, thus quantitatively connecting charge carrier decomposition to capacity fade. 48

The data in Figure 4a show selected UV-vis spectra of a 5 mM DMeQUIC electrolyte during a 16 h potentiostatic reduction in a DMeQUIC-Fe(CN)₆ flow cell. DMeQUIC peaks at 245, 325, and 335 nm fell within the first 2 min of reduction, at the expense of a broad peak centered at 365 nm, which rose and grew until 10 min, before falling gradually afterward. The diminution of the 365 nm peak coincided with the emergence of two new peaks at 235 and 293 nm.

Bayesian inference determined that the time-varying absorbance profiles in Figure 4a are well explained by the successive evolution of three unique species, whose pure spectra and temporal concentrations are shown in Figures 4b and S6, respectively. Given the cell cycling data in Section 3.1, we interpret the pure spectra to represent DMeQUIC, its reduced form (rDMQ), a transient but redox-active decay product of the reduced form (tDMQ), and a final redoxinactive species (fDMQ). From the concentration profiles, first-order rate constants for the conversion of DMeQUIC to rDMQ, rDMQ to tDMQ, and tDMQ to fDMQ were calculated to be 2.0×10^{-2} , 9.5×10^{-5} , and 1.4×10^{-5} s⁻¹, respectively. First-order kinetics was supported by similar rates of molecular conversion upon reduction of DMeQUIC at concentrations of 4, 3, and 1 mM (Figure S7a-d). The concentration independence of these rates is inconsistent with DMeQUIC decay being rate-limited by a bimolecular mechanism such as dimerization.

The spectroscopically-derived rate constants are quantitatively consistent with the capacity fade rates in Figure 2b. Assuming that capacity loss during shallow-discharge cycling is controlled by conversion of rDMQ to tDMQ yields a rate constant for that process of $1.8 \times 10^{-4} \text{ s}^{-1}$ (see Figure S8, eqs S1 and S2, and accompanying discussion), which agrees well with the corresponding value from spectroscopic/Bayesian analysis on the 5 mM DMeQUIC data. A similar estimation of the rate constant for conversion of tDMQ to fDMQ from cycling to the lower discharge potential of -0.1 V yields $2.2 \times$ 10⁻⁵ s⁻¹, which is again in good agreement with the analogous value from the Bayesian analysis of the spectra.

Analysis of electrochemically reduced DMeQUIC solutions using NMR spectroscopy and liquid chromatography-mass spectrometry (LC-MS) revealed that tautomerization accounted for the observed decomposition. Figure S9 displays a

two-dimensional correlation spectroscopy (2D COSY) ¹H NMR spectrum of a DMeQUIC solution after full reduction in a flow cell and storage under an inert (nitrogen) atmosphere for 1 week (to permit the complete conversion of rDMQ to fDMQ). The signal previously observed at 3.8 ppm in Figure 3e was found to be coupled to the three-proton signal at 1 ppm. We interpret this coupling to indicate that the proton represented by the 3.8 ppm signal is bonded to a carbon adjacent to the methyl carbon, which is consistent with the enamine-imine tautomerization of reduced DMeQUIC (Figure 5). Tautomer formation is further supported by ¹³C NMR

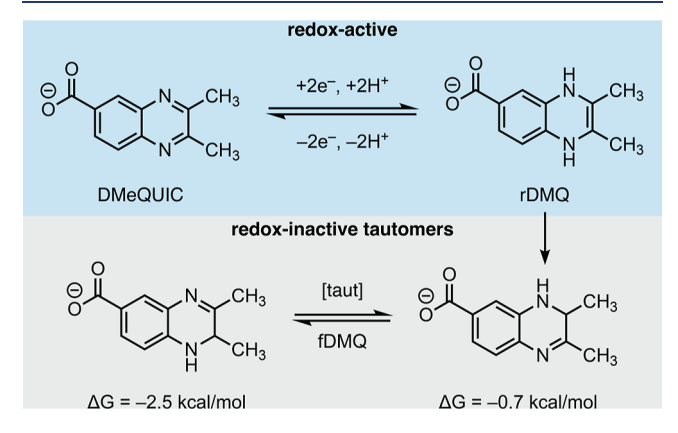


Figure 5. Redox reaction that converts DMeQUIC to rDMQ and subsequent tautomerization of rDMQ into redox-inactive tautomers fDMQ. Tautomerization free energies calculated by DFT at pH 13, 1 M species, and 298 K are indicated.

spectra of the same solutions (Figure S10). Uncycled DMeQUIC has no peaks between 30 and 120 ppm (Figure S10a), whereas reduced DMeQUIC has a peak at 48 ppm (Figure S10b) which is consistent with the presence of an sp³hybridized carbon bonded to N, as would occur in the tautomers in Figure 5. LC-MS (Figure S11a,b) provided additional evidence for tautomerization and against other potential decomposition mechanisms, such as Michael addition (Figure S12a) and full hydrogenation of the pyrazine core (Figure S12b). The DMeQUIC spectrum displayed the strongest peak at m/z = 201.0652, which is justified by its molar mass of 202.2130 g/mol and the deprotonation of the carboxylic acid group. The spectrum for reduced DMeQUIC displayed the strongest peak at m/z = 203.0803 (Figure S11b), which is explained by the net addition of two hydrogen atoms

to DMeQUIC via two-electron reduction and concerted/stepwise protonation. This m/z value is consistent with tautomerization because the intramolecular transfer of a hydrogen atom will not change m/z. An m/z of 203.0803 is, however, inconsistent with a Michael addition product (molar mass = 222.2440 g/mol) or full hydrogenation of the pyrazine core in DMeQUIC (molar mass = 206.2450 g/mol). To further rule out the fully hydrogenated species, we purchased the fully reduced quinoxaline as an authentic standard and observed distinct 1 H and 13 C NMR spectra compared to the observed decomposition product (Figure S13a,b). These findings are in line with previous reports of enamine-imine tautomerization of quinoxalines 37,62 and pyridopyrazines 63 after electrochemical reduction in alkaline media.

Although the above data support the idea that fDMQ is a tautomer of rDMQ (Figure 5), the exact structure of the intermediate tDMQ is not known. Nevertheless, it is plausible that tDMQ and fDMQ have similar chemical structures given that their Bayesian-inferred UV—vis spectra (Figure 4b) are almost identical and that the tautomer proton is present in the NMR spectra of the reduced form of DMeQUIC shortly after reduction (Figure 3e) and after 1 week of storage in an inert atmosphere (Figure S14). One possibility is that tDMQ is the deprotonated form of fDMQ, which is supported by previous work on phenacylquinolines showing that under alkaline conditions imine-enamine tautomerization can proceed via a deprotonated imine intermediate.⁶⁴

3.3. Effect of Functionalization on Tautomerization **Energetics.** We performed DFT modeling to elucidate the effect of functionalization on reduced quinoxaline tautomerization and quinoxaline stability. Previous work has shown that the equilibrium between enamine and imine forms of reduced quinoxalines in nonaqueous media can be strongly dependent on solvent and substituent chemistry. 65 For the five molecules that we study experimentally in Section 3.4, shown in Figure 6a, tautomerization is predicted to be exothermic for the reduced forms of DMeQUI and DMeQUIC, whereas it is slightly endothermic for 6QUIC and DMeSQUI (~2 kcal/ mol) and highly endothermic (~10 kcal/mol) for 2QUIC (Figure S15 and Figure S16). Generally, Michael addition (Figure S17) is predicted to be endothermic and is typically less thermodynamically favorable compared with tautomerization (Figure S15), consistent with our experimental observations. Likewise, dimerization of the quinoxaline derivatives was computed to be generally very endothermic (e.g., 55.9, 52.1, 53.6, and 48.4 kcal/mol for the reduced forms of 2QUIC, 6QUIC, DMeQUIC, and DMeQUI, respectively). We discuss three molecular properties that influence the tautomerization energetics and its link to molecular structure: (1) redox potential, (2) relative pK_a values of the enamine and imine forms and their connection to the electron-withdrawing group (EWG) strength of quinoxaline functional groups, and (3) hydrogen bonding between the pyrazine N-H and an Hacceptor functional group.

In addition to the experimentally tested derivatives, we also computationally modeled 13 other derivatives, including quinoxaline-2,3-disulfonic acid-6-carboxylic acid (DS6QUIC), quinoxaline (QUI), 2-acetylquinoxaline (2COCH3QUI), quinoxaline-2,3-dicarbonitrile (DCNQUI), quinoxaline-5-carboxylic acid (5QUIC), quinoxaline-5,8-dicarboxylic acid (5,8-QUIDC), quinoxaline-2,3-dicarbonitrile-6,7-disulfonic acid (DCNQUI-6,7-DS), quinoxaline-2-carbonitrile (2CNQUI), 2-nitroquinoxaline (2NO2QUI), quinoxaline-2-amine

(2NQUI), 3-amino-quinoxaline-2-carboxylic acid (QUI2C3A), 2-methylquinoxaline (2MeQUI), and quinoxaline-2-carbaldehyde (2CHOQUI), as shown in Figure 6b. The data in Figure 6c show the DFT-computed redox potentials at pH 13 against the free energy of tautomerization for all 18 quinoxalines. We identify a weak but positive correlation between the redox potential and tautomerization energy (R^2 = 0.49), revealing a trade-off between a high open-circuit potential and resistance to tautomerization. The DFTcalculated redox potentials of the experimentally studied quinoxalines (indicated by red squares in Figure 6c), which lie between -0.8 and -1.2 V versus Ag/AgCl at pH 13, agree moderately well with experimentally determined values. Intuitively, the redox potential and tautomerization energy are related to the strength of the N-H bond of the pyrazine ring, which is modulated by the functional groups. A stronger N-H bond makes tautomerization from the enamine to the imine form more unfavorable because this process requires breaking the N-H bond and forming a C-H bond. In addition, it makes reduction, which involves the formation of the N-H bond, more favorable. Our analysis suggests that a strong N-H bond leads to favorable reduction, a more positive redox potential, and less favorable tautomerization.

Hammett analysis reveals a relationship between the EWG strength of the quinoxaline substituents and the tautomerization energetics. Quinoxaline derivatives with stronger EWGs have a more stable enamine form relative to the imine form, making tautomerization less favorable. The Hammett plot in Figure 6d shows the effect of the σ^- Hammett constant of the substituent adjacent to the pyrazine N (substituent R in Figure S4) and the tautomerization free energy when there are no substituents in any other positions (that is, when only substituent R is changed). Hammett substituent constants are taken from Hansch and co-workers.⁶⁶ Because we hypothesize that tautomerization occurs via a deprotonated intermediate, we use the σ^- Hammett constant as a measure of the ability of a substituent to strengthen the resonance stabilization of a negatively charged intermediate via its electron-withdrawing capacity. A positive correlation exists between σ^- and tautomerization energy ($R^2 = 0.66$), meaning that a stronger EWG in the position adjacent to pyrazine N would result in a greater resistance to tautomerization. A similar relationship has been observed between the σ_n or σ_m Hammett constant and tautomerization equilibrium for 3amylcarbamoylmethylene-2-oxo-1,2,3,4-tetrahydroquinoxalines. 65 This effect can be explained by the influence of EWGs on the pK_a values of the enamine and imine forms of the reduced quinoxaline derivative in question.

By definition, the negative base-10 logarithm of the tautomerization equilibrium constant is equal to the pK_a value of the N–H proton of the enamine minus the pK_a of the unsaturated C–H proton of the imine (see eq S7 and Figure S4 in the Supporting Information for derivation). Although DMeQUIC has an electron-donating group, the inductive effect of an EWG stabilizes the deprotonated intermediate tDMQ (Figure S16), thereby lowering the pK_a of the enamine. Because tDMQ is a resonance structure of the deprotonated imine, its stabilization also lowers the pK_a of the imine. However, stronger EWGs, which lead to a more positive tautomerization energy (Figure 6d), lower the pK_a of the imine approximately eight times as much as they lower the pK_a of the enamine, as supported by our DFT calculations (Figure 6e). For example, the enamine and imine forms of quinoxaline

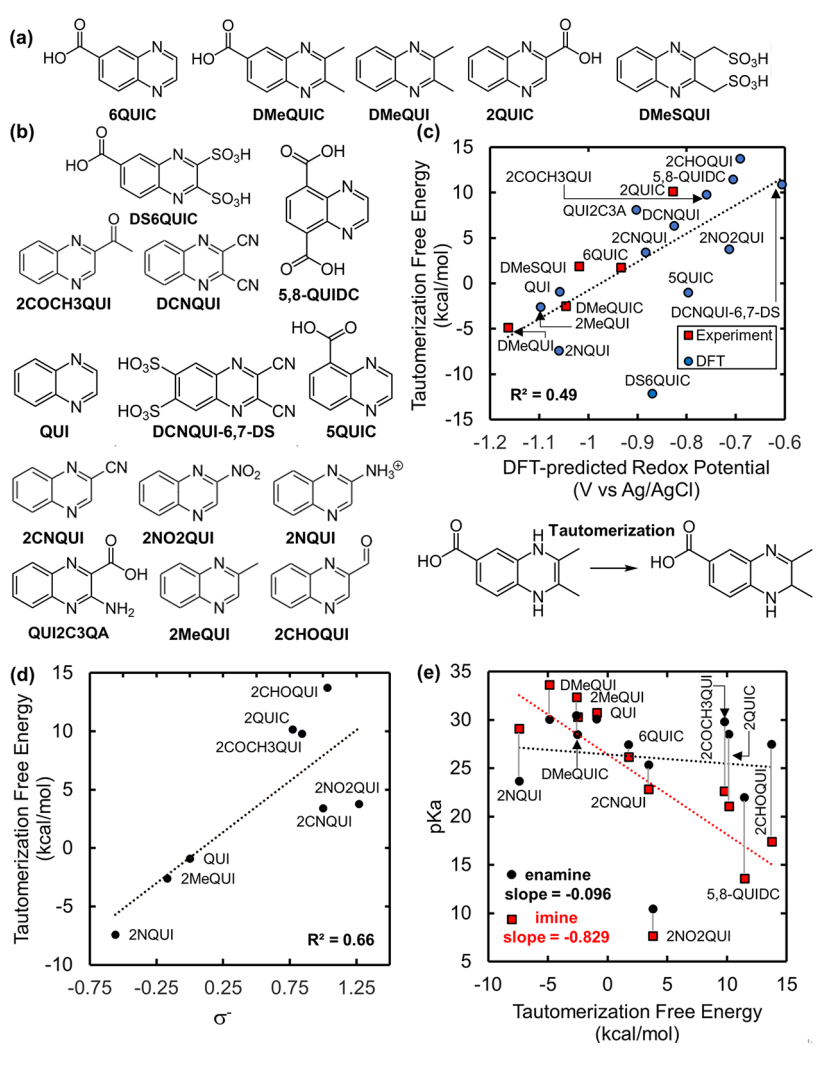


Figure 6. (a) Molecules studied by DFT modeling that are cycled experimentally. (b) Molecules not experimentally cycled but also evaluated by DFT modeling. (c) Relationship between DFT-computed tautomerization free energy and DFT-computed redox potential at pH 13, 1 M species, and 298 K. Data points of molecules studied experimentally are indicated by red squares and other molecules evaluated only by DFT by blue circles. Tautomerization of DMeQUIC from the enamine to the imine form is shown schematically as an example, with other derivatives in (a) and (b) tautomerizing analogously. (d) Relationship between σ^- Hammett constant of the substituent in the position adjacent to pyrazine N and tautomerization energy for quinoxaline derivatives functionalized only in the position adjacent to the pyrazine N. (e) Comparison of DFT-calculated tautomerization energy and p K_a values of imine (red squares) and enamine (black circles) forms of quinoxaline derivatives. Vertical gray lines are given to highlight the difference between the p K_a values of the enamine and imine forms. Slopes of trendlines fitting p K_a of the enamine (in black) or imine form (in red) as a function of tautomerization energy are indicated.

(QUI) have pK_a values of 30.1 and 30.8, respectively. Upon substitution of an EWG in the position adjacent to the pyrazine N ($-COCH_3$, -COOH, or -CHO), the enamine pK_a drops slightly (to 29.8, 28.5, and 27.5, respectively), while the imine pK_a drops significantly (to 22.6, 21.1, and 17.4, respectively). Alternatively, the substitution of an electrondonating methyl group at the same position increases the enamine and imine pK_a values to 30.5 and 32.4, respectively. This nonsymmetric effect on the relative pK_a values occurs because the pyrazine N is closer to the aromatic ring, and therefore its deprotonated form is more resonance-stabilized compared to the carbanion without the effect of an EWG. Consequently, the stabilizing effect of an EWG is more pronounced on the carbanion (or deprotonated imine), explaining the asymmetric effect on the pK_a values of the imine and enamine manifested as the different slopes in Figure 5e. Similar effects have been observed for the enol-keto

tautomerism of β -diketones and β -ketoesters and α -arylsulphaminopyridines. 8

Another factor that results in unfavorable tautomerization is the stabilization of the enamine structure by forming a hydrogen bond between the H on the pyrazine N and a hydrogen bond acceptor group in an adjacent substituent, which may contribute to the stability of 2QUIC to tautomerization. Also, because only one of the two pyrazine N-H groups of 5QUIC is hydrogen-bonded to the carboxylic acid group, only one of the two possible tautomerization pathways requires breaking the hydrogen bond. This pathway is associated with an unfavorable free energy change (+8.6 kcal/mol), in contrast to a slightly favorable free energy change associated with the alternative pathway that does not break the hydrogen bond (-1.0 kcal/mol). This observation suggests that the formation of a hydrogen bond with both pyrazine H atoms would enable strong resistance to tautomerization, and indeed, 5,8-QUIDC has a DFT-calculated tautomerization free

energy of +11.5 kcal/mol, more unfavorable than that for SQUIC. In theory, the two carboxylic acid groups of 5,8-QUIDC make this molecule not only resistant to tautomerization but also highly soluble; therefore, it is a potentially promising derivative for resisting capacity fade in aqueous organic redox flow batteries.

3.4. Flow Cell Cycling of Other Quinoxaline Derivatives. We experimentally evaluated the influence of functionalization on the cycling stability of a subset of quinoxaline derivatives (Figure 6a) analyzed by DFT. DMeQUIC, DMeQUI, 6QUIC, and 2QUIC were procured commercially, whereas DMeSQUI was synthesized for this study via a simple, one-step reaction (synthetic procedures are reported in Section 2.6, whereas CV and NMR characterization data are reported in the Supporting Information). The other derivatives analyzed by DFT that have endothermic tautomerization energies are not commercially available, with the exception of QUI2C3A. The CV of QUI2C3A displayed a 1.1 V separation between cathodic and anodic redox peaks (Figure S18), which renders cycling of this molecule in a flow battery impractical.

Cycling results are shown in Figure S19a, which reports capacity (normalized to the theoretical capacity for a two-electron reduction) versus time for cycling at the current densities and voltage limits provided in Table S2. First-order capacity fade rate constants were estimated from the slope of the line of best fit for normalized discharge capacity on a logarithmic scale against time (Figure S19b), and were found to vary over 3 orders of magnitude (Table 1), increasing in the

Table 1. CV-Derived Standard Redox Potentials of Experimentally Tested Quinoxaline Derivatives and Capacity Fade Rate Constants from Flow Cell Cycling

molecule	fade rate constant (s ⁻¹)	redox potential (V vs Ag/AgCl)
2QUIC	$5.31 \pm 0.04 \times 10^{-7}$	-0.95
DMeSQUI	$4.33 \pm 0.05 \times 10^{-6}$	-1.01
DMeQUI	$2.71 \pm 0.07 \times 10^{-5}$	-1.10
DMeQUIC	$8.9 \pm 0.2 \times 10^{-5}$	-1.12
6QUIC	$3.5 \pm 0.1 \times 10^{-4}$	-1.00

following order: 2QUIC < DMeSQUI < DMeQUI < DMeQUIC < 6QUIC. We conducted CV measurements of all cycled electrolytes (Figure S20a—e) and discovered a strong correlation between the decrease in peak cathodic current and capacity lost during flow cell cycling (Figure S21).

DFT-predicted tautomerization energetics rationalize experiments for quinoxaline stability; for example, the most stable derivative tested, 2QUIC, was predicted to have very endothermic tautomerization ($\Delta G_{\text{taut}} = +10.2 \text{ kcal/mol}$), whereas the less stable molecules such as DMeQUIC and 6QUIC had values of ΔG_{taut} of -2.5 and 1.8 kcal/mol, respectively. We avoid quantitatively correlating tautomerization energetics to measured decay rates because the predicted thermodynamic driving force does not directly consider kinetic barriers, which can play a critical role in driving tautomerization.³⁷ Nevertheless, it is worth noting that the 4.6%/day capacity fade rate for the 2QUIC cell is about 2 orders of magnitude slower than that of DMeQUIC (Figure 7), which demonstrates that functionalization can play an important role in stabilizing quinoxalines against tautomerization upon reduction.

Because the permeability of Nafion to organic charge carriers under aqueous conditions translates to a capacity fade rate

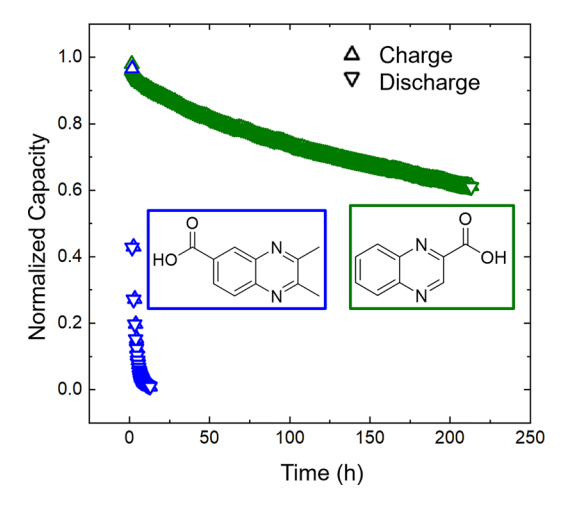


Figure 7. Normalized charge and discharge capacity during CCCV cycling of compositionally asymmetric flow cells containing 0.4 M of DMeQUIC (shallow-discharge cycling) and 0.4 M 2QUIC in the capacity-limiting electrolyte and ferrocyanide in the non-capacity-limiting electrolyte. The electrolyte composition for the DMeQUIC cell is provided in Figure 2. The capacity-limiting side of the 2QUIC cell comprised 3 mL of 0.4 M 2QUIC with 0.5 M NaOH, whereas the non-capacity-limiting side comprised 20 mL of 0.4 M Na $_4$ Fe(CN) $_6$ and 0.1 M NaOH.

constant of up to ca. $6 \times 10^{-7}~{\rm s}^{-1},^{69,70}$ we evaluated the possibility that molecular crossover rather than decomposition accounted for most of the apparent capacity fade in the 2QUIC cell. The permeability of Nafion 212 to 2QUIC was measured using an H-cell to be $2.5 \times 10^{-9}~{\rm cm}^2/{\rm s}$ (Figure S22a–c). Based on this permeability (calculated using eq S8), capacity fade from crossover would be about 6.9%/day, which is close to the 4.6%/day fade rate measured in the 2QUIC cell. Future studies may address the issue of crossover using tailored membranes. 70,71

To assess the intrinsic chemical stability of 2QUIC, we cycled a volumetrically unbalanced, compositionally symmetric cell⁴² that contained 0.05 M 2QUIC (Figure 8). It exhibited a capacity fade rate of 0.005%/day over 65 h of CCCV cycling. To our knowledge, this rate is the lowest ever measured for a quinoxaline derivative and is comparable to fade rates measured for aqueous flow cells capacity-limited by the most stable previously reported negolytes (Figure S23). A list of recently reported organic molecules exhibiting a range of fade rates during cell cycling, including those with a capacity fade rate of <0.1%/day, along with 2QUIC, is provided in Table S2. 2QUIC has a lower equivalent weight and a more negative redox potential compared to virtually all of these molecules (Figure S24), which may lower costs at the system level. 15 We also cycled a mixed symmetric cell that was capacity-limited by 2QUIC but had 2QUIC and ferrocyanide on both sides to limit crossover-induced capacity fade. The cell had an opencircuit potential of 1.2 V and did not exhibit capacity fade (Figure 9a) over 220 h of CCCV cycling between 0.8 and 1.4 V. It rather showed a small increase in capacity that cumulatively amounted to <1% of the initial redox capacity of 2QUIC. The increase is equivalent to a gain in volume of about 30 μ L and might have been caused by slow entrainment of initially stranded electrolyte into the main flow circuit. CVs of 2QUIC in the cycled and uncycled electrolytes from the capacity-limiting side of the cell (Figure S25) were virtually identical, indicating negligible change in the redox capacity of

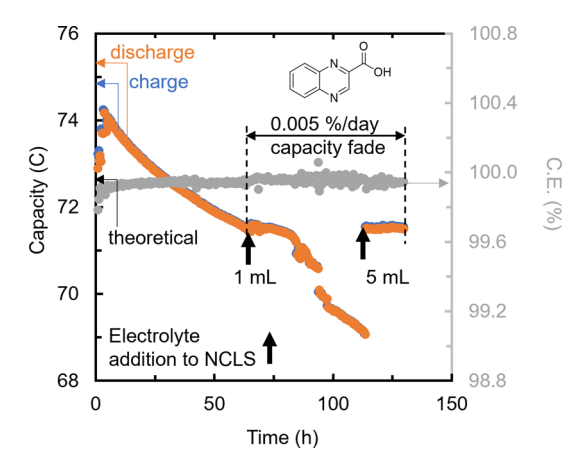


Figure 8. Charge capacity, discharge capacity, and Coulombic efficiency vs time during cycling of a compositionally symmetric 2QUIC cell. The capacity-limiting side initially comprised a halfreduced (50% SOC) solution of 7.5 mL of 0.05 M 2QUIC and 1 M NaOH; the non-capacity-limiting side comprised 18 mL of the same composition. The two sides were separated by a Nafion 212 membrane, and the cell was cycled with a CCCV protocol with each half cycle terminating when the current reached an absolute value of 1 mA/cm². The capacity fade during the first 65 h of cycling was only apparent because additions of 50% SOC aliquots of the 0.05 M 2QUIC (upward-pointing arrows) to the non-capacity-limiting side resulted in capacity recovery and a reduction in the capacity loss rate. The choice of potential limits had no effect on the cell's capacity or capacity loss rate: ±0.3 V was applied for the first 41 h, ±0.2 V between 41 and 65 h, ± 0.3 V between 65 and 97 h, and ± 0.35 V between 97 and 130 h. The cell exhibited a very low capacity fade rate of 0.005%/day between the two additions to the non-capacity-limiting side. The capacity fade observed before 65 h can therefore be attributed to cell imbalance.7

the electrolyte. Although low 2QUIC concentrations (\leq 0.1 M) were used in the foregoing cycling measurements, it is likely that 2QUIC can be cycled at higher concentrations. We measured 2QUIC solubilities of 0.45 and 1.22 M in 1 M NaOH and 1 M KOH, respectively (Figure S26), the latter of which translates to a high volumetric capacity of 65 A h/L. As a whole, our cycling studies validate the design principles for tautomerization-resistant quinoxalines described in Section 3.3

and motivate the continued pursuit of quinoxaline derivatives that combine high chemical stability with fast kinetics, high solubility, and low redox potential.

4. CONCLUSIONS

pubs.acs.org/JACS

Quinoxalines are a class of redox-active molecules that have several attractive attributes as charge carriers in aqueous RFBs but have been hindered in these systems because of their stability issues. Understanding the substituent impact on quinoxaline stability and thus capacity fade would aid in the further development of these molecules for RFB systems that have long lifetimes and thus deliver electricity at low costs.

We study the cycling stability of 2,3-dimthylquinoxaline-6carboxylic acid (DMeQUIC) and discover that tautomerization of its reduced form is chiefly responsible for the observed capacity fade. Data from several complementary analytical techniques—including operando UV—vis spectroscopy, ¹H NMR spectroscopy, ¹³C NMR spectroscopy, and mass spectrometry, rule out other mechanisms that have been proposed in the literature for quinoxaline degradation, such as dimerization, irreversible hydrogenation, and Michael addition of water. Bayesian inference is shown to be a useful technique to estimate, while accounting for uncertainty, the rate constants of quinoxaline tautomerization and deconvolution of the pure UV-vis spectra of the resulting products from operando spectroscopic measurements. Quantitative consistency between the kinetic parameters estimated from spectroscopy and the rates of capacity fade measured at the cell level highlights the unique ability of combining Bayesian inference and operando UV-vis spectroscopy to elucidate the connection between molecular decomposition and capacity fade.

Using DFT modeling, we elucidate multiple design rules (i.e., tuning electron-withdrawing group strength and H-bonding strength) for tautomerization resistance in quinoxalines and identify more stable derivatives with those properties—the most stable among experimentally tested derivatives is quinoxaline-2-carboxylic acid (2QUIC), which yielded a capacity fade rate of 0.005%/day when cycled in a volumetrically unbalanced, compositionally symmetric cell and no measurable capacity fade in a mixed symmetric cell configuration. In a compositionally asymmetric cell config-

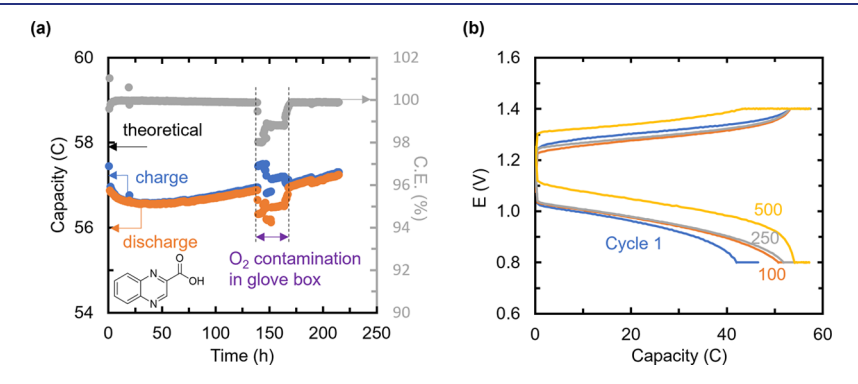


Figure 9. (a) Charge capacity, discharge capacity, and Coulombic efficiency vs time and (b) voltage profiles of selected cycles for the cycling of a mixed symmetric 2QUIC-ferrocyanide cell for 220 h. The capacity-limiting side of the cell comprised 3 mL of 0.1 M 2QUIC, 0.2 M $Na_4Fe(CN)_6$, and 0.2 M NaOH; the non-capacity-limiting side comprised 7 mL of the same solution. The cell was cycled at a current density of 20 mA/cm² between 0.8 and 1.4 V, and potential holds were applied at the end of each half cycle until the current density decayed to an absolute value of 1 mA/cm². The dip in current efficiency between 140 and 170 h, from an average of 99.9% to 98%, was due to momentary contamination of the glovebox by oxygen. Parasitic oxygen reduction in the capacity-limiting side led to the accumulation of ferricyanide in the non-capacity-limiting side and thus led to an increase in cell potential between cycles 250 and 500 in Figure 9b.

uration with a Nafion 212 membrane, crossover-induced capacity fade was high (ca. 5%/day), likely due to the small molecular size of 2QUIC. Future work may address this issue via the development of membranes with higher permselectivity than Nafion or the installation of multiple charged substituents to slow down crossover without overly compromising the stability or synthesizability of the quinoxaline.

These findings will guide the development of stable quinoxalines in aqueous RFBs and may also be extended toward the discovery of high-performing pyrazine derivatives, which have more negative redox potentials than quinoxalines. Additionally, the combination of experimental and statistical inference techniques demonstrated in this work is broadly adaptable to studying degradation mechanisms and capacity loss for other organic redox-active molecules.

ASSOCIATED CONTENT

Data Availability Statement

Computational data for this paper, including NWChem input and output files, are available in the NOMAD Repository at 10.17172/NOMAD/2023.09.08-1.

Supporting Information

The Supporting Information is available free of charge at https://pubs.acs.org/doi/10.1021/jacs.3c10454.

Synthesis and characterization data, Bayesian inference analysis, and computational details (PDF)

AUTHOR INFORMATION

Corresponding Author

David G. Kwabi — Department of Mechanical Engineering, University of Michigan, Ann Arbor, Michigan 48109, United States; orcid.org/0000-0003-3663-8789; Email: dkwabi@umich.edu

Authors

Sanat Vibhas Modak — Department of Mechanical Engineering, University of Michigan, Ann Arbor, Michigan 48109, United States; orcid.org/0000-0002-3822-8794

Daniel Pert – Department of Chemical Engineering, University of Michigan, Ann Arbor, Michigan 48109, United States

Jessica L. Tami – Department of Chemistry, University of Michigan, Ann Arbor, Michigan 48109, United States; orcid.org/0000-0003-3106-5790

Wanggang Shen — Department of Mechanical Engineering, University of Michigan, Ann Arbor, Michigan 48109, United States

Ibrahim Abdullahi – Department of Mechanical Engineering, University of Michigan, Ann Arbor, Michigan 48109, United States

Xun Huan – Department of Mechanical Engineering, University of Michigan, Ann Arbor, Michigan 48109, United States; orcid.org/0000-0001-6544-2764

Anne J. McNeil — Department of Chemistry, University of Michigan, Ann Arbor, Michigan 48109, United States; Macromolecular Science and Engineering Program, University of Michigan, Ann Arbor, Michigan 48109, United States; orcid.org/0000-0003-4591-3308

Bryan R. Goldsmith — Department of Chemical Engineering, University of Michigan, Ann Arbor, Michigan 48109, United States; Occid.org/0000-0003-1264-8018

Complete contact information is available at: https://pubs.acs.org/10.1021/jacs.3c10454

Notes

The authors declare no competing financial interest.

ACKNOWLEDGMENTS

This work was funded by the National Science Foundation under award number 2033969. The research also used resources from the National Energy Research Scientific Computing Center, a DOE Office of Science User Facility supported by the Office of Science of the U.S. Department of Energy, under Contract no. DE-AC02-05CH11231 using NERSC award BES-ERCAP0021451. A.J.M., J.L.T. and B.R.G. acknowledge support from the Microsoft Climate Research Initiative. We would like to thank Basilio Suherman and Fairooz Oudeif for assistance with NMR measurements.

■ REFERENCES

- (1) Soloveichik, G. L. Flow Batteries: Current Status and Trends. Chem. Rev. 2015, 115, 11533-11558.
- (2) Li, Z.; Pan, M. S.; Su, L.; Tsai, P.-C.; Badel, A. F.; Valle, J. M.; Eiler, S. L.; Xiang, K.; Brushett, F. R.; Chiang, Y.-M. Air-breathing aqueous sulfur flow battery for ultralow-cost long-duration electrical storage. *Joule* **2017**, *1*, 306–327.
- (3) Brushett, F. R.; Aziz, M. J.; Rodby, K. E. On lifetime and cost of redox-active organics for aqueous flow batteries. *ACS Energy Lett.* **2020**, *5*, 879–884.
- (4) Ziegler, M. S.; Mueller, J. M.; Pereira, G. D.; Song, J.; Ferrara, M.; Chiang, Y.-M.; Trancik, J. E. Storage requirements and costs of shaping renewable energy toward grid decarbonization. *Joule* **2019**, *3*, 2134–2153.
- (5) Dieterich, V.; Milshtein, J. D.; Barton, J. L.; Carney, T. J.; Darling, R. M.; Brushett, F. R. Estimating the cost of organic battery active materials: a case study on anthraquinone disulfonic acid. *Transl. Mater. Res.* **2018**, *5*, 034001.
- (6) Kwabi, D. G.; Ji, Y.; Aziz, M. J. Electrolyte lifetime in aqueous organic redox flow batteries: a critical review. *Chem. Rev.* **2020**, *120*, 6467–6489.
- (7) Kwabi, D.; Lin, K.; Ji, Y.; Kerr, E.; Goulet, M.-A.; De Porcellinis, D.; Tabor, D.; Pollack, D.; Aspuru-Guzik, A.; Gordon, R.; Aziz, M. Alkaline Quinone Flow Battery with Long Lifetime at pH 12. *Joule* **2018**, 2, 1907–1908.
- (8) Ji, Y.; Goulet, M.-A.; Pollack, D. A.; Kwabi, D. G.; Jin, S.; De Porcellinis, D.; Kerr, E. F.; Gordon, R. G.; Aziz, M. J. A phosphonate-functionalized quinone redox flow battery at near-neutral pH with record capacity retention rate. *Adv. Energy Mater.* **2019**, *9*, 1900039.
- (9) Jin, S.; Jing, Y.; Kwabi, D. G.; Ji, Y.; Tong, L.; De Porcellinis, D.; Goulet, M.-A.; Pollack, D. A.; Gordon, R. G.; Aziz, M. J. A watermiscible quinone flow battery with high volumetric capacity and energy density. *ACS Energy Lett.* **2019**, *4*, 1342–1348.
- (10) Hoober-Burkhardt, L.; Krishnamoorthy, S.; Yang, B.; Murali, A.; Nirmalchandar, A.; Prakash, G. K. S.; Narayanan, S. A new Michael-reaction-resistant benzoquinone for aqueous organic redox flow batteries. *J. Electrochem. Soc.* **2017**, *164*, A600—A607.
- (11) Xu, J.; Pang, S.; Wang, X.; Wang, P.; Ji, Y. Ultrastable aqueous phenazine flow batteries with high capacity operated at elevated temperatures. *Joule* **2021**, *5*, 2437–2449.
- (12) Wang, C.; Li, X.; Yu, B.; Wang, Y.; Yang, Z.; Wang, H.; Lin, H.; Ma, J.; Li, G.; Jin, Z. Molecular design of fused-ring phenazine derivatives for long-cycling alkaline redox flow batteries. *ACS Energy Lett.* **2020**, *5*, 411–417.
- (13) Wellala, N. P.; Hollas, A.; Duanmu, K.; Murugesan, V.; Zhang, X.; Feng, R.; Shao, Y.; Wang, W. Decomposition pathways and mitigation strategies for highly-stable hydroxyphenazine flow battery anolytes. *J. Mater. Chem. A* **2021**, *9*, 21918–21928.
- (14) Darling, R. M. Techno-economic analyses of several redox flow batteries using levelized cost of energy storage. *Curr. Opin. Chem. Eng.* **2022**, *37*, 100855.

- (15) Gregory, T. D.; Perry, M. L.; Albertus, P. Cost and price projections of synthetic active materials for redox flow batteries. *J. Power Sources* **2021**, 499, 229965.
- (16) Akhil, A. A.; Huff, G.; Currier, A. B.; Kaun, B. C.; Rastler, D. M.; Chen, S. B.; Cotter, A. L.; Bradshaw, D. T.; Gauntlett, W. D. DOE/EPRI 2013 Electricity Storage Handbook in Collaboration with NRECA, 2013.
- (17) Tong, F.; Yuan, M.; Lewis, N. S.; Davis, S. J.; Caldeira, K. Effects of Deep Reductions in Energy Storage Costs on Highly Reliable Wind and Solar Electricity Systems. *iScience* **2020**, 23, 101484
- (18) Sepulveda, N. A.; Jenkins, J. D.; Edington, A.; Mallapragada, D. S.; Lester, R. K. The design space for long-duration energy storage in decarbonized power systems. *Nat. Energy* **2021**, *6*, 506–516.
- (19) Wang, C.; Wang, Y.; Tao, M.; Yu, B.; Zhang, K.; Wei, J.; Liu, Y.; Zhang, P.; Ding, G.; Tie, Z.; et al. Highly water-soluble 6-quinoxalinecarboxylic acid for high-voltage aqueous organic redox flow batteries. ACS Appl. Energy Mater. 2022, 5, 10379–10384.
- (20) Pasadakis-Kavounis, A.; Baj, V.; Hjelm, J. Electrochemical Characterization of Aromatic Molecules with 1, 4-Diaza Groups for Flow Battery Applications. *Molecules* **2021**, *26*, 2227.
- (21) Leung, P.; Aili, D.; Xu, Q.; Rodchanarowan, A.; Shah, A. Rechargeable organic—air redox flow batteries. *Sustainable Energy Fuels* **2018**, 2, 2252—2259.
- (22) Milshtein, J. D.; Su, L.; Liou, C.; Badel, A. F.; Brushett, F. R. Voltammetry study of quinoxaline in aqueous electrolytes. *Electrochim. Acta* **2015**, *180*, 695–704.
- (23) Leung, P.; Shah, A.; Sanz, L.; Flox, C.; Morante, J.; Xu, Q.; Mohamed, M.; Ponce de León, C.; Walsh, F. Recent developments in organic redox flow batteries: A critical review. *J. Power Sources* **2017**, 360, 243–283.
- (24) Brushett, F. R.; Vaughey, J. T.; Jansen, A. N. An all-organic non-aqueous lithium-ion redox flow battery. *Adv. Energy Mater.* **2012**, 2, 1390–1396.
- (25) Nageswar, Y.; Reddy, K. H. V.; Ramesh, K.; Murthy, S. N. Recent developments in the synthesis of quinoxaline derivatives by green synthetic approaches. *Org. Prep. Proced. Int.* **2013**, *45*, 1–27.
- (26) Yashwantrao, G.; Saha, S. Recent advances in the synthesis and reactivity of quinoxaline. *Org. Chem. Front.* **2021**, *8*, 2820–2862.
- (27) Parvez, M. M.; Haraguchi, N.; Itsuno, S. Molecular design of chiral quaternary ammonium polymers for asymmetric catalysis applications. *Org. Biomol. Chem.* **2012**, *10*, 2870–2877.
- (28) Jing, Y.; Zhao, E. W.; Goulet, M.-A.; Bahari, M.; Fell, E. M.; Jin, S.; Davoodi, A.; Jónsson, E.; Wu, M.; Grey, C. P.; et al. In situ electrochemical recomposition of decomposed redox-active species in aqueous organic flow batteries. *Nat. Chem.* **2022**, *14*, 1103–1109.
- (29) Carino, E. V.; Diesendruck, C. E.; Moore, J. S.; Curtiss, L. A.; Assary, R. S.; Brushett, F. R. BF3-promoted electrochemical properties of quinoxaline in propylene carbonate. *RSC Adv.* **2015**, *5*, 18822–18831.
- (30) Ames, J. R.; Houghtaling, M. A.; Terrian, D. L. Cyclic voltammetry of some quinoxaline di-N-oxides and quinoxalines in dimethylformamide. *Electrochim. Acta* 1992, *37*, 1433–1436.
- (31) Barqawi, K.; Atfah, M. A cyclic voltammetric study of some quinoxaline di-n-oxides and quinoxalines in acetonitrile: substituent effect on the cathodic reduction. *Electrochim. Acta* **1987**, 32, 597–599.
- (32) Angulo, G.; Dobkowski, J.; Kapturkiewicz, A.; Maciolek, K. Photophysics and electrochemistry of quinoxaline chromophores decorated with thiophene or furane subunits. *J. Photochem. Photobiol., A* **2010**, 213, 101–106.
- (33) Kaur, A. P.; Holubowitch, N. E.; Ergun, S.; Elliott, C. F.; Odom, S. A. A highly soluble organic catholyte for non-aqueous redox flow batteries. *Energy Technol.* **2015**, *3*, 476–480.
- (34) Yan, N.; Li, G.; Gao, X. Electroactive organic compounds as anode-active materials for solar rechargeable redox flow battery in dual-phase electrolytes. *J. Electrochem. Soc.* **2014**, *161*, A736–A741.
- (35) Armand, J.; Boulares, L.; Bellec, C.; Pinson, J. Electrochemical reduction of quinoxalino[2,3-b]quinoxaline. *Can. J. Chem.* **1982**, *60*, 2797–2803.

- (36) Armand, J.; Boulares, L.; Bellec, C.; Pinson, J. Preparation, chemical and electrochemical reduction of pyrido[2,3-b]quinoxalines and pyrido[3,4-b]quinoxalines. *Can. J. Chem.* **1988**, *66*, 1500–1505.
- (37) Armand, J.; Bellec, C.; Boulares, L.; Chaquin, P.; Masure, D.; Pinson, J. Electrochemical and chemical reduction of furopyrazines, thienopyrazines, furoquinoxalines and thienoquinoxalines. *J. Org. Chem.* **1991**, *56*, 4840–4845.
- (38) Narayan, S. R.; Nirmalchandar, A.; Murali, A.; Yang, B.; Hoober-Burkhardt, L.; Krishnamoorthy, S.; Prakash, G. S. Nextgeneration aqueous flow battery chemistries. *Curr. Opin. Electrochem.* **2019**, *18*, 72–80.
- (39) Aleksic, M.; Pantic, J.; Kapetanovic, V. Evaluation of kinetic parameters and redox mechanism of quinoxaline at glassy carbon electrode. *Facta Univ., Ser.: Phys., Chem. Technol.* **2014**, *12*, 55–63.
- (40) Chen, Q.; Eisenach, L.; Aziz, M. J. Cycling analysis of a quinone-bromide redox flow battery. *J. Electrochem. Soc.* **2016**, *163*, A5057–A5063.
- (41) Barton, J. L.; Milshtein, J. D.; Hinricher, J. J.; Brushett, F. R. Quantifying the impact of viscosity on mass-transfer coefficients in redox flow batteries. *J. Power Sources* **2018**, 399, 133–143.
- (42) Goulet, M.-A.; Aziz, M. J. Flow battery molecular reactant stability determined by symmetric cell cycling methods. *J. Electrochem. Soc.* **2018**, *165*, A1466–A1477.
- (43) Andrieu, C.; de Freitas, N.; Doucet, A.; Jordan, M. I. An Introduction to MCMC for Machine Learning. *Mach. Learn.* **2003**, *50*, 5–43.
- (44) Handbook of Markov Chain Monte Carlo; Brooks, S., Gelman, A., Jones, G., Meng, X.-L., Eds.; Chapman and Hall/CRC, 2011
- (45) Metropolis, N.; Rosenbluth, A. W.; Rosenbluth, M. N.; Teller, A. H.; Teller, E. Equation of State Calculations by Fast Computing Machines. *J. Chem. Phys.* **1953**, *21*, 1087–1092.
- (46) Hastings, W. K. Monte Carlo sampling methods using Markov chains and their applications. *Biometrika* **1970**, *57*, 97–109.
- (47) Salvatier, J.; Wiecki, T. V.; Fonnesbeck, C. Probabilistic programming in Python using PyMC3. *PeerJ Comput. Sci.* **2016**, 2, No. e55.
- (48) Modak, S. V.; Shen, W.; Singh, S.; Herrera, D.; Oudeif, F.; Goldsmith, B. R.; Huan, X.; Kwabi, D. G. Understanding capacity fade in organic redox-flow batteries by combining spectroscopy with statistical inference techniques. *Nat. Commun.* **2023**, *14*, 3602.
- (49) Valiev, M.; Bylaska, E. J.; Govind, N.; Kowalski, K.; Straatsma, T. P.; Van Dam, H. J. J.; Wang, D.; Nieplocha, J.; Apra, E.; Windus, T. L.; de Jong, W. A. NWChem: A comprehensive and scalable open-source solution for large scale molecular simulations. *Comput. Phys. Commun.* **2010**, *181*, 1477–1489.
- (50) Lee, C.; Yang, W.; Parr, R. G. Development of the Colle-Salvetti correlation-energy formula into a functional of the electron density. *Phys. Rev. B* **1988**, *37*, 785–789.
- (51) Becke, A. D. Density-functional thermochemistry. III. The role of exact exchange. *J. Chem. Phys.* **1993**, *98*, 5648–5652.
- (52) Weigend, F.; Ahlrichs, R. Balanced basis sets of split valence, triple zeta valence and quadruple zeta valence quality for H to Rn: Design and assessment of accuracy. *Phys. Chem. Chem. Phys.* **2005**, *7*, 3297–3305.
- (53) Klamt, A.; Schüürmann, G. COSMO: a new approach to dielectric screening in solvents with explicit expressions for the screening energy and its gradient. *J. Chem. Soc., Perkin Trans.* **1993**, 2, 799–805.
- (54) York, D. M.; Karplus, M. A Smooth Solvation Potential Based on the Conductor-Like Screening Model. *J. Phys. Chem. A* **1999**, *103*, 11060–11079.
- (55) Dutra, F. R.; Silva, C. d. S.; Custodio, R. On the Accuracy of the Direct Method to Calculate pKa from Electronic Structure Calculations. *J. Phys. Chem. A* **2021**, *125*, 65–73.
- (56) Wertz, D. H. Relationship between the gas-phase entropies of molecules and their entropies of solvation in water and 1-octanol. *J. Am. Chem. Soc.* **1980**, *102*, 5316–5322.

- (57) Ding, M.; Fu, H.; Lou, X.; He, M.; Chen, B.; Han, Z.; Chu, S.; Lu, B.; Zhou, G.; Jia, C. A stable and energy-dense polysulfide/permanganate flow battery. *ACS Nano* **2023**, *17*, 16252–16263.
- (58) Saraidaridis, J.; Yang, Z. Electrolyte Takeover Strategy for Performance Recovery in Polysulfide-Permanganate Flow Batteries. *J. Electrochem. Soc.* **2021**, *168*, 110556.
- (59) Yang, Z.; Gerhardt, M. R.; Fortin, M.; Shovlin, C.; Weber, A. Z.; Perry, M. L.; Darling, R. M.; Saraidaridis, J. D. Polysulfide-Permanganate Flow Battery Using Abundant Active Materials. *J. Electrochem. Soc.* **2021**, *168*, 070516.
- (60) Modak, S.; Valle, J.; Tseng, K.-T.; Sakamoto, J.; Kwabi, D. G. Correlating stability and performance of NaSICON membranes for aqueous redox flow batteries. ACS Appl. Mater. Interfaces 2022, 14, 19332–19341.
- (61) Colli, A. N.; Peljo, P.; Girault, H. H. High energy density MnO4-/MnO42- redox couple for alkaline redox flow batteries. *Chem. Commun.* **2016**, 52, 14039–14042.
- (62) Armand, J.; Boulares, L.; Bellec, C.; Pinson, J. Electrochemical reduction of quinoxalino [2, 3-b] quinoxaline. *Can. J. Chem.* **1982**, *60*, 2797–2803.
- (63) Armand, J.; Boulares, L.; Bellec, C.; Pinson, J. Preparation, chemical and electrochemical reduction of pyrido [2, 3-b] quinoxalines and pyrido [3, 4-b] quinoxalines. *Can. J. Chem.* **1988**, *66*, 1500–1505.
- (64) Carey, A. R. E.; Fukata, G.; O'Ferrall, R. A. M.; Murphy, M. G. The mechanism of imine—enamine tautomerism of 2-and 4-phenacylquinolines. *J. Chem. Soc., Perkin Trans.* 1985, 2, 1711–1722.
- (65) Kurasawa, Y.; Miyashita, R.; Takada, A.; Kim, H. S.; Okamoto, Y. Substituent effects on the tautomer ratios between the enamine and methylene imine forms in side-chained quinoxalines. *J. Heterocycl. Chem.* **1995**, 32, 671–674.
- (66) Hansch, C.; Leo, A.; Taft, R. W. A survey of Hammett substituent constants and resonance and field parameters. *Chem. Rev.* **1991**, *91*, 165–195.
- (67) Sandler, I.; Harper, J. B.; Ho, J. Explanation of Substituent Effects on the Enolization of β -Diketones and β -Ketoesters. *J. Chem. Educ.* **2021**, *98*, 1043–1048.
- (68) Mastrukova, T. A.; Sheinker, Y. N.; Kuznetsova, I. K.; Peresleni, E. M.; Sakharova, T. B.; Kabachnik, M. I. The application of the Hammett equation to the theory of tautomeric equilibrium—II: Tautomerism of α -arylsulphaminopyridines. *Tetrahedron* **1963**, *19*, 357–372.
- (69) Murali, A.; Nirmalchandar, A.; Krishnamoorthy, S.; Hoober-Burkhardt, L.; Yang, B.; Soloveichik, G.; Prakash, G. K. S.; Narayanan, S. Understanding and mitigating capacity fade in aqueous organic redox flow batteries. *J. Electrochem. Soc.* **2018**, *165*, A1193—A1203.
- (70) George, T. Y.; Kerr, E. F.; Haya, N. O.; Alfaraidi, A. M.; Gordon, R. G.; Aziz, M. J. Size and Charge Effects on Crossover of Flow Battery Reactants Evaluated by Quinone Permeabilities Through Nafion. *J. Electrochem. Soc.* **2023**, *170*, 040509.
- (71) Zuo, P.; Ye, C.; Jiao, Z.; Luo, J.; Fang, J.; Schubert, U. S.; McKeown, N. B.; Liu, T. L.; Yang, Z.; Xu, T. Near-frictionless ion transport within triazine framework membranes. *Nature* **2023**, *617*, 299–305.
- (72) Fell, E. M.; De Porcellinis, D.; Jing, Y.; Gutierrez-Venegas, V.; George, T. Y.; Gordon, R. G.; Granados-Focil, S.; Aziz, M. J. Long-Term Stability of Ferri-/Ferrocyanide as an Electroactive Component for Redox Flow Battery Applications: On the Origin of Apparent Capacity Fade. *J. Electrochem. Soc.* **2023**, *170*, 070525.